


Thermal suppression of demixing dynamics in a binary condensate

Vijay Pal Singh ^{1,2} Luigi Amico,^{1,3,4,*} and Ludwig Mathey^{2,5}

¹Quantum Research Centre, Technology Innovation Institute, Abu Dhabi 9639, United Arab Emirates

²Zentrum für Optische Quantentechnologien and Institut für Laserphysik, Universität Hamburg, 22761 Hamburg, Germany

³INFN-Sezione di Catania, Via S. Sofia 64, 95127 Catania, Italy

⁴Centre for Quantum Technologies, National University of Singapore, 117543 Singapore, Singapore

⁵The Hamburg Centre for Ultrafast Imaging, Luruper Chaussee 149, 22761 Hamburg, Germany



(Received 11 April 2023; accepted 9 August 2023; published 13 October 2023)

We investigate the demixing dynamics in a binary two-dimensional (2D) Bose superfluid using classical-field dynamics. By quenching the interspecies interaction parameter, we identify a strong and weak separation regime depending on the system temperature and the quench parameter. In the strong separation regime our results are in agreement with the inertial hydrodynamic domain growth law of binary fluids and a Porod scaling law for the structure factor at zero temperature is found. In the weak separation regime thermal fluctuations modify both the domain growth law and the Porod tail of the structure factor. Near the superfluid transition temperature the scaling dynamics approaches the diffusive growth law of a 2D conserved field. We then analyze the demixing dynamics in a box cloud. For low quench we find distinctive domain dynamics dictated by the boundary condition. Otherwise, the dynamics are qualitatively similar to those of systems with periodic boundary conditions.

DOI: [10.1103/PhysRevResearch.5.043042](https://doi.org/10.1103/PhysRevResearch.5.043042)

I. INTRODUCTION

When two immiscible fluids such as water and oil are allowed to mix, they separate into two distinct phases [1]. Such phase separation phenomenon is very well established in science, with relevant implications for important technological applications [2–4]. In physics, phase separation occurs in a variety of condensed matter systems such as polymers, fluid mixtures, gels, ferroelectrics, membranes, superfluids, superconductors, and the like.

According to classical theories of phase-ordering dynamics, the domain growth follows a characteristic power-law behavior $L(t) \sim t^\eta$, where L is the average domain size and η is the scaling exponent. The dynamics is universal such that the time evolution of an observable is solely governed by $L(t)$. In practice, this scaling hypothesis is tested by the equal-time correlation function $C(\mathbf{r}', t) = \langle \phi(\mathbf{r} + \mathbf{r}', t) \phi(\mathbf{r}, t) \rangle$, where $\phi(\mathbf{r})$ is an order parameter characterizing the dynamical evolution of the system and $\langle \dots \rangle$ denotes the statistical average. The Fourier transform of $C(\mathbf{r}, t)$ is the structure factor $S(\mathbf{k}, t) = \langle \phi_{\mathbf{k}}(t) \phi_{-\mathbf{k}}(t) \rangle$, where $\phi_{\mathbf{k}}$ is the Fourier transform of $\phi(\mathbf{r})$. From a dimensional consideration the structure factor obeys the scaling relation $S(k, t) = L^d f(kL(t))$ [5], where d is the spatial dimensionality and the scaling function $f(q)$ is independent of time. Due to the presence of domain walls,

$f(q)$ exhibits a power-law tail $f(q) \sim q^{-(d+1)}$ at large q , which is referred to as the Porod law [6]. The scaling theory hypothesizes various power laws for domain coarsening, which describe the time dependence of characteristic length scales. The domain growth law for a two-dimensional (2D) conserved field is $L \sim t^{1/3}$, which characterizes the diffusive transport of the order parameter [5,7,8]. In binary fluids a competition between the viscous and inertial flow leads to two growth regimes: viscous hydrodynamic ($L \sim t$) [9] and inertial hydrodynamic ($L \sim t^{2/3}$) [10]. The viscous hydrodynamic regime has been confirmed by experiments as well as simulations [5]. However, the inertial hydrodynamic regime has not been observed yet as viscous flow is non-negligible in classical fluids.

Ultracold atoms have emerged as an ideal platform to study the dynamics of multicomponent superfluids, forming the basis for the study of a multitude of phenomena such as the miscible-immiscible transition in binary fluids [11–14]. Experimentally, Bose-Bose mixtures using different hyperfine levels or different isotopes have been used to study phase separation [15–18], nonlinear dynamical excitations [19–22], solitons [23,24], and Townes solitons [25]. Domain formation and coarsening were observed in quenched immiscible mixtures [26]. Following the proposal [27], Rabi-coupled Bose mixtures [28] were used to experimentally test the Kibble-Zurek mechanism [29]. Theoretically, many studies reported dynamical scaling laws in superfluid systems [30–39] and dynamical instabilities [40–46]. It was pointed out that thermal fluctuations suppress the phase separation at nonzero temperatures [47–49]. The inertial hydrodynamic regime was investigated theoretically in binary 2D superfluids [34,50]. Nevertheless, many features of dynamical scaling such as the role of thermal fluctuations are yet to be explored.

*On leave from Dipartimento di Fisica e Astronomia “Ettore Majorana”, University of Catania, Catania, Italy.

Published by the American Physical Society under the terms of the [Creative Commons Attribution 4.0 International license](https://creativecommons.org/licenses/by/4.0/). Further distribution of this work must maintain attribution to the author(s) and the published article’s title, journal citation, and DOI.

In this paper, we investigate how the thermal fluctuations influence the dynamical scaling of coarsening in a binary 2D Bose superfluid. To this end, we employ semiclassical-field simulations to address the demixing dynamics at nonzero temperature, which is triggered by quenching the immiscibility parameter $\alpha = g_{12}/\sqrt{g_{11}g_{22}}$, where g_{12} is the interspecies interaction, and g_{11} and g_{22} are the intraspecies interactions. As a key result, we show how the characteristic scaling of domain growth is modified by the temperature and the quench parameter. The interplay of the quench and thermal energy results in two phase separation regimes. The first one is the strong separation regime that occurs at low temperature and $\alpha \gtrsim 1.4$, for which the Porod scaling law of the structure factor $S(k) \sim k^{-3}$ holds, and the domain coarsening follows the inertial hydrodynamic growth law of binary fluids, i.e., $L(t) \sim t^{2/3}$. The other regime is the weak separation regime at high temperatures, where thermal fluctuations modify both the domain growth law and the Porod tail of the structure factor. Near the superfluid critical temperature the domain coarsening approaches the diffusive growth law of a 2D conserved field ($L \sim t^{1/3}$) and the Porod tail of the structure factor scales close to $S(k) \sim k^{-1}$. Furthermore, we examine the demixing dynamics in a box cloud and find an intriguing interplay of the box symmetry and the dynamics. In particular, for α close to 1 and small clouds, with sizes comparable to the spin healing length, demixing occurs via the creation of domains of regular patterns due to the boundary condition. For high α and large clouds we recover the dynamics that is similar to the system with periodic boundary conditions.

II. SYSTEM AND METHODOLOGY

We consider a cloud of ^{87}Rb atoms in two different hyperfine states $|F=1, m_F=0\rangle$ and $|F=2, m_F=0\rangle$, which is motivated by the experiments [51,52]. Thus, the two species have the same masses ($m_1 = m_2 = m$) and the intraspecies scattering lengths are $a_{11}/a_B = 100.86$ and $a_{22}/a_B = 94.58$ [53], where a_B is the Bohr radius. The interspecies scattering length is $a_{12}/a_B = 98.9$ [54], resulting in the parameter $\alpha = 1.012$, which is defined as

$$\alpha \equiv a_{12}/\sqrt{a_{11}a_{22}}. \quad (1)$$

Since α is slightly above 1, the two species are weakly immiscible and thermal fluctuations play a prominent role in the demixing dynamics, as we show below. In our theoretical study we vary α in the range $1.03 \leq \alpha \leq 1.55$ to examine both weakly and strongly immiscible regimes, which covers a wide range of immiscible regime that can be explored with mixtures of other species, in addition to ^{87}Rb , which provided the experimental motivation of this study. We describe the system by the Hamiltonian

$$\hat{H} = \hat{H}_1 + \hat{H}_2 + \hat{H}_{12}, \quad (2)$$

with

$$\hat{H}_a = \int d\mathbf{r} \left[\left(\frac{\hbar^2}{2m_a} \nabla \hat{\psi}_a^\dagger(\mathbf{r}) \cdot \nabla \hat{\psi}_a(\mathbf{r}) + \frac{g_{aa}}{2} \hat{\psi}_a^\dagger(\mathbf{r}) \hat{\psi}_a^\dagger(\mathbf{r}) \hat{\psi}_a(\mathbf{r}) \hat{\psi}_a(\mathbf{r}) \right) \right] \quad (3)$$

and

$$\hat{H}_{12} = \int d\mathbf{r} [g_{12} \hat{\psi}_1^\dagger(\mathbf{r}) \hat{\psi}_2^\dagger(\mathbf{r}) \hat{\psi}_2(\mathbf{r}) \hat{\psi}_1(\mathbf{r})], \quad (4)$$

where $a = 1, 2$ represent the two species and $\hat{\psi}_a$ ($\hat{\psi}_a^\dagger$) are the corresponding annihilation (creation) operators. The intraspecies interactions g_{aa} and interspecies interaction g_{12} are given by, respectively,

$$g_{aa} = \frac{2\sqrt{2\pi}\hbar^2}{m} \frac{a_{aa}}{\ell_z} \quad \text{and} \quad g_{12} = \frac{2\sqrt{2\pi}\hbar^2}{m} \frac{a_{12}}{\ell_z}. \quad (5)$$

$\ell_z = \sqrt{\hbar/(m\omega_z)}$ is the harmonic oscillator length of the trapping potential in the transverse direction, where ω_z is the trap frequency. We note that to avoid unwanted buoyancy effect, the alignment of the 2D gas as orthogonal to gravity has to be achieved sufficiently well, and with sufficiently strong transverse confinement. For a condensate with a large number of atoms we replace $\hat{\psi}_a$ by complex numbers ψ_a . Using Eq. (2) we obtain the coupled equations of motion

$$i\hbar\partial_t\psi_1 = \left(-\frac{\hbar^2}{2m}\nabla^2 + g_{11}n_1 + g_{12}n_2 \right) \psi_1, \quad (6)$$

$$i\hbar\partial_t\psi_2 = \left(-\frac{\hbar^2}{2m}\nabla^2 + g_{22}n_2 + g_{12}n_1 \right) \psi_2, \quad (7)$$

which govern the dynamics of binary condensates. $n_a = |\psi_a|^2$ are the densities. This system hosts two excitation branches of collective modes [55]

$$E_{k,\pm}^2 = \frac{(E_1^2 + E_2^2)}{2} \pm \frac{1}{2} \sqrt{(E_1^2 - E_2^2)^2 + 16\epsilon_k^2 n_1 n_2 g_{12}^2}, \quad (8)$$

where $E_a = \sqrt{\epsilon_k(\epsilon_k + 2g_{aa}n_a)}$ are the single-component Bogoliubov spectra and $\epsilon_k = \hbar^2 k^2 / (2m)$. The coupling g_{12} results in hybridized branches $E_{k,\pm}$. A direct consequence of this hybridization is that the low-momentum part of $E_{k,-}$ vanishes when $\alpha = 1$ (or equivalently $g_{12} = \sqrt{g_{11}g_{22}}$) and becomes imaginary for $\alpha > 1$. This leads to the creation of unstable modes when α is above 1, which is responsible for the demixing of the two species. We note that $\alpha_c = 1$ is the quantum critical point separating the miscible ($\alpha < \alpha_c$) and immiscible ($\alpha > \alpha_c$) states at zero temperature [13]. The range of unstable modes is determined by setting $E_{k,-} = 0$, giving (see Appendix A)

$$k_0^2 = \frac{1}{\xi_1^2 \xi_2^2} \left[\sqrt{(\xi_1^2 - \xi_2^2)^2 + 4\alpha^2 \xi_1^2 \xi_2^2} - (\xi_1^2 + \xi_2^2) \right], \quad (9)$$

where $\xi_a = \hbar/\sqrt{2mg_{aa}n_a}$ are the single-component healing lengths. k_0 vanishes when $\alpha = 1$ and increases with increasing α for $\alpha > 1$. The wavelength $\lambda_0 = 2\pi/k_0$ and the lifetime $\tau = \hbar/E_{k_0,-}$ give an estimate of length and time scale for the emergence of domains.

We investigate the phase-separation dynamics using the classical-field method of Refs. [56,57]. For the numerical simulations we discretize the space on a lattice of size $N_x \times N_y$ and a discretization length $l = 1 \mu\text{m}$. We note that l is chosen to be smaller than or comparable to the healing length and the thermal de Broglie wavelength [58]. This maps the continuum Hamiltonian on the discrete Bose-Hubbard model, which introduces $J = \hbar^2/(2ml^2)$ as the tunneling energy and $U_{aa} = g_{aa}l^{-2}$ and $U_{12} = g_{12}l^{-2}$ as the on-site repulsive interactions.

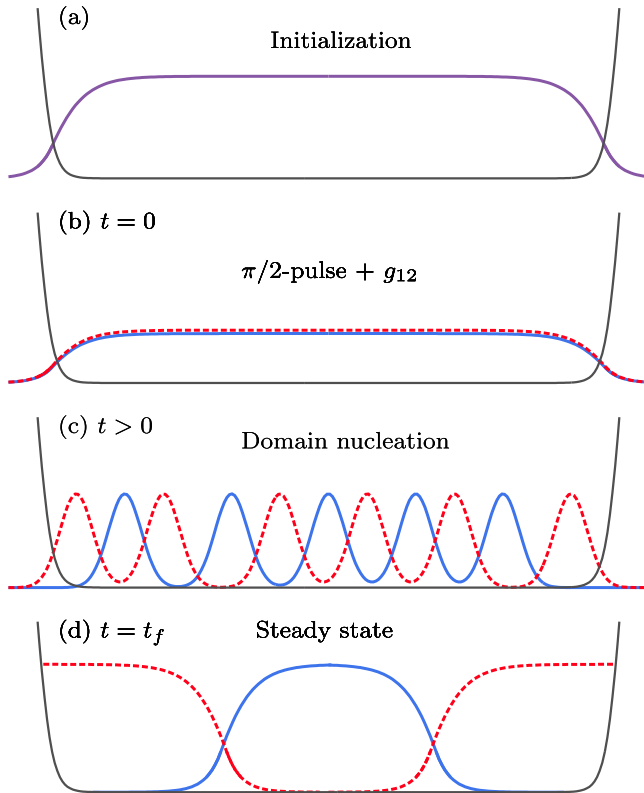


FIG. 1. Sketch of the quench protocol for a homogeneous cloud confined in a box potential. (a) The initial state is a thermal state having total density n at temperature T . (b) We apply a $\pi/2$ pulse to obtain a uniform superposition of species 1 (dashed line) and 2 (continuous line). Thereafter, we quench the interspecies interaction g_{12} into the demixed regime, which creates a dynamically unstable mixture of two species. (c) Time evolution proceeds via nucleation of domains of species 1 and 2. (d) Long-time evolution at final time t_f results in a steady state having species 2 at the center and species 1 forming a shell around it.

We use $\omega_z = 2\pi \times 4.6$ kHz, leading to $U_{11}/J = 0.336$ and $U_{22}/U_{11} = 0.938$ [51]. The quench protocol is described in

Fig. 1. We start with a 2D superfluid cloud of total density $n = 10 \mu\text{m}^{-2}$ at temperature T . The initial states $\psi_1(\mathbf{r})$ of this system are sampled in a grand-canonical ensemble of chemical potential μ and temperature T via a classical Metropolis algorithm [56]. We choose T in a wide range of $T/T_0 = 0.1-1.1$, where T_0 is an estimate of the critical temperature for the superfluid transition in weakly interacting 2D Bose gases [59,60]. For the other species we sample the initial states with vacuum fluctuations, i.e., $\langle |\psi_2(\mathbf{r}_i)|^2 \rangle = 1/(2l^2)$ [61], where the index i corresponds to the lattice site and $\langle \dots \rangle$ denotes the ensemble average. At time $t = 0$ we use a $\pi/2$ pulse to obtain a uniform superposition of the states $\psi_{1/2}(\mathbf{r}_i) = [\psi_1(\mathbf{r}_i) \pm \psi_2(\mathbf{r}_i)]/\sqrt{2}$. This results in the two cloud densities $n_1 \approx n_2 \approx n/2 = 5 \mu\text{m}^{-2}$, since g_{11} and g_{22} are similar. We then quench g_{12} in the demixed regime ($\alpha > 1$) and determine the time evolution $\psi_{1/2}(\mathbf{r}, t)$ via Eqs. (6) and (7). As schematically shown in Figs. 1(c) and 1(d), the initial time evolution proceeds via nucleation of small-sized domains and the long-time evolution results in two spatially separated clouds. To analyze the demixing dynamics, as an order parameter, we calculate the local density imbalance

$$m(\mathbf{r}, t) = \frac{n_1(\mathbf{r}, t) - n_2(\mathbf{r}, t)}{n_1(\mathbf{r}, t) + n_2(\mathbf{r}, t)}. \quad (10)$$

We show $m(\mathbf{r}, t)$ for a periodic-boundary system in Fig. 2 and its average $\langle m(\mathbf{r}, t) \rangle$ for a box system in Fig. 6, where $\langle \dots \rangle$ denotes an average over the initial ensemble.

III. RESULTS

A. Demixing dynamics

In Fig. 2 we show the time evolution of $m(\mathbf{r}, t)$ of a single trajectory at $T/T_0 = 0.21$ for $\alpha = 1.03$ and 1.55. We employ a fixed system size of $256 \times 256 \mu\text{m}^2$ for all periodic-boundary simulations. The quench to the demixed state at $t = 0$ triggers the nucleation of domains of each component, where smaller domains during the initial formation are present for $\alpha = 1.55$ than that for $\alpha = 1.03$. We estimate the initial domain size L_0 by the momentum range k_0 of unstable modes in Eq. (9). We obtain $L_0 \sim \lambda_0 = 19$ and $4.7 \mu\text{m}$ and the nucleation time $t \sim$

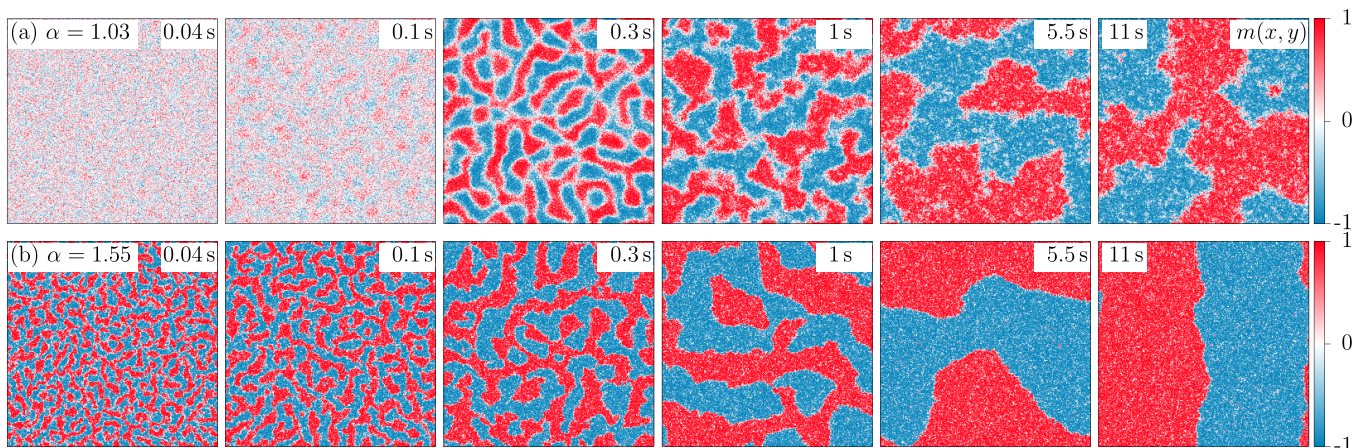


FIG. 2. Nucleation of domains and the coarsening dynamics. Time evolution of the two-species density imbalance $m(x, y)$ of a single trajectory for $\alpha = 1.03$ (upper row) and 1.55 (lower row), displaying nucleation of domains of two components (red and blue) and their coarsening dynamics. The spatial dimensions for each panel are $256 \times 256 \mu\text{m}^2$.

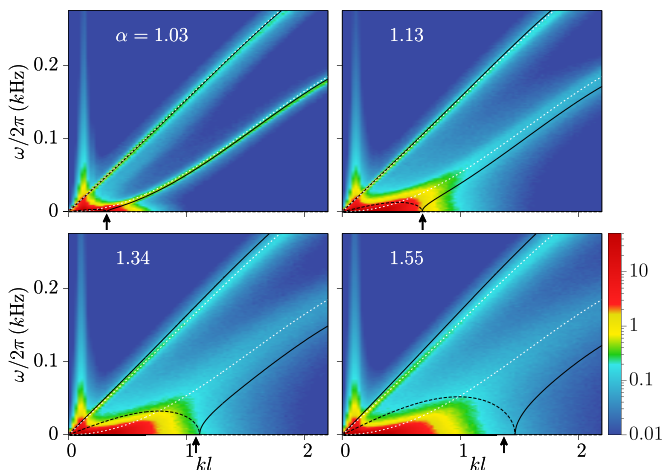


FIG. 3. Nonequilibrium excitation spectra. Dynamic structure factor $S_1(\mathbf{k}, \omega)$ as a function of the wave vector $\mathbf{k} = k\hat{\mathbf{e}}_x$ and frequency ω for $\alpha = 1.03, 1.13, 1.34,$ and 1.55 . The black continuous lines are the Bogoliubov spectra $E_{k,\pm}$ of Eq. (8) and the black dashed line represents the imaginary part of $E_{k,-}$. The arrow indicates the momentum range of unstable modes based on Eq. (9), which is derived for continuous space. In our numerically discretized space representation, this prediction is modified toward the solution of Eq. (A4), resulting in a deviation from Eq. (9); see also the discussion in Appendix A. The white dotted lines correspond to the spectra of phase-separated clouds; see text.

$\tau = 26$ ms and 1.5 ms for $\alpha = 1.03$ and 1.55 , respectively. The intermediate time evolution manifests the coarsening process, where small domains shrink and large ones grow. There are small patches of other component in the domains, which are due to the initial fluctuations that suppress the dynamics in the weak separation regime. This is the scenario for $\alpha = 1.03$, whereas for $\alpha = 1.55$ the dynamics is weakly affected by these fluctuations as the system is in the strong separation regime. The weak versus strong separation regime occurs as an interplay between the thermal and quench energy. At high temperatures thermal fluctuations dominate the dynamics and no phase separation occurs as we show in Appendix B.

To identify the interplay of collective modes in the demixing dynamics we calculate the dynamic structure factor of the density

$$S_1(\mathbf{k}, \omega) = \langle |n_1(\mathbf{k}, \omega)|^2 \rangle, \quad (11)$$

where $n_1(\mathbf{k}, \omega)$ is the Fourier transform of the density $n_1(\mathbf{r}, t)$ of component 1 in space and time:

$$n_1(\mathbf{k}, \omega) = \frac{1}{\sqrt{N_x T_s}} \sum_j \int_0^{T_s} dt e^{-i(\mathbf{k}\mathbf{r}_j - \omega t)} n_1(\mathbf{r}_j, t). \quad (12)$$

T_s is the sampling time for the numerical Fourier transform and $N_l = N_x N_y$ is the number of lattice sites. We choose the same $T_s = 0.55$ s for all α , where the choice of T_s is based on a time window that includes both nucleation and coarsening of domains; see also Appendix C. In Fig. 3 we show $S_1(\mathbf{k}, \omega)$ as a function of the wave vector $\mathbf{k} = k\hat{\mathbf{e}}_x$ and

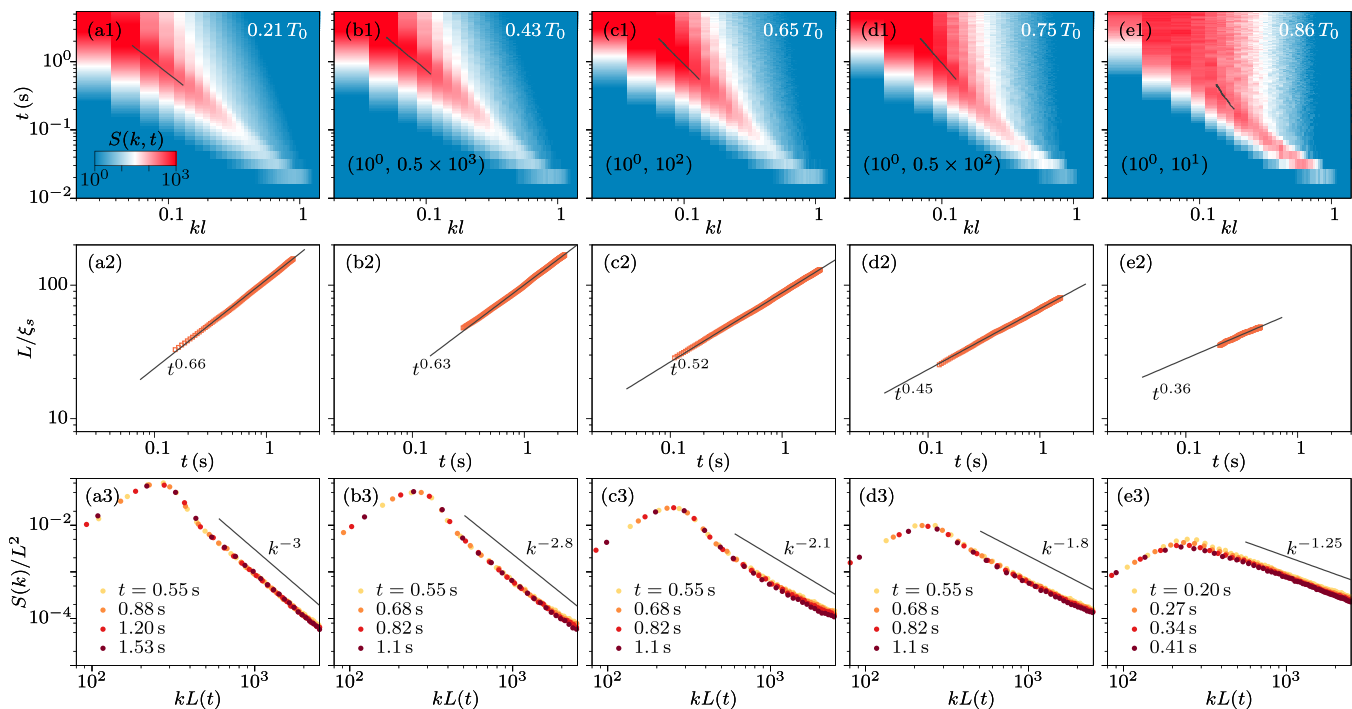


FIG. 4. Growth laws and dynamical scaling at nonzero temperatures. (a1)–(e1) Structure factor $S(\mathbf{k}, t)$ as a function of the wave vector $\mathbf{k} = k\hat{\mathbf{e}}_x$ and time t on a log-log scale for $\alpha = 1.55$ and various T/T_0 . The upper and lower ranges of spectral weights for (b1)–(e1) are given in parentheses. The location of the maximum (continuous line) allows us to determine the average domain size $L(t)$; see text. (a2)–(e2) The values of $L(t)$ and their power-law t^η fit (line) yield $\eta = 0.66, 0.63, 0.52, 0.45,$ and 0.36 for $T/T_0 = 0.21, 0.43, 0.65, 0.75,$ and 0.86 , respectively. ξ_s is the spin healing length; see text. (a3)–(e3) Plots of $S(k)/L^2$ versus $kL(t)$ demonstrate universal time evolution for various t . The continuous line indicates an approximate scaling for the high-momentum tail.

frequency ω for $\alpha = 1.03, 1.13, 1.34,$ and 1.55 . We observe both dynamically stable and unstable modes, where stable modes appear as two excitation branches and unstable ones as a broad spectrum of low-energy excitation. We compare these results with the Bogoliubov spectra $E_{k,\pm}$ of Eq. (8). For our discretized system, the free-particle dispersion takes the form $\epsilon_k = 2J[1 - \cos(k_x l)]$, where $J = \hbar^2/(2ml^2)$ is the tunneling energy. We show the real-valued predictions of $E_{k,\pm}$ as the continuous lines in Fig. 3, which capture the excitation branches of stable modes for low and intermediate α and show deviations for high α . We also show the imaginary solution of $E_{k,-}$, which qualitatively captures the broad spectrum of unstable modes. The momentum range of unstable modes increases with increasing α and is close to the predictions of Eq. (9). There is a peaklike excitation at small k corresponding to the structure of a macroscopic domain that the system forms at time $t = T_s$, which shifts to a lower k at high α ; see the structure factor shown in Appendix C. This implies the development of large domains at high α in agreement with the dynamics presented in Fig. 2.

Furthermore, we compare the two excitation branches of stable modes with the spectra of phase-separated clouds. In this case, the cloud density is twice the initial density, i.e., $n_{i,f} = 2n_i$, and the Bogoliubov spectrum reads $E_{k,n_{i,f}} = \sqrt{\epsilon_k(\epsilon_k + 2g_{11}n_{i,f})}$. This result agrees with the upper branch of $S_1(k, \omega)$ for all α in Fig. 3. The other component being spatially separated from component 1 acts as a thermal cloud whose free-particle dispersion captures the lower branch for all α in Fig. 3.

B. Dynamical scaling

To characterize the scaling behavior we calculate the structure factor of the imbalance

$$S(\mathbf{k}) = \langle |m(\mathbf{k})|^2 \rangle, \quad (13)$$

with

$$m(\mathbf{k}) = \frac{1}{\sqrt{N_l}} \sum_j \exp(-i\mathbf{k}\mathbf{r}_j) m(\mathbf{r}_j), \quad (14)$$

where $m(\mathbf{k})$ is the Fourier transform of $m(\mathbf{r})$. In Figs. 4(a1)–4(e1) we show $S(\mathbf{k}, t)$ as a function of the wave vector $\mathbf{k} = k\hat{\mathbf{e}}_x$ and time t for $\alpha = 1.55$ and various T/T_0 . The nucleation of domains is indicated by the spectral peak at finite k , which gradually moves to smaller k as the domains coarsen. The location of the peak describes an average size of the domain, whereas the peak broadening reflects the influence of thermal fluctuations on the dynamics. The thermal effect is strong at high temperature, resulting in a decreasing peak amplitude in Figs. 4(a1)–4(e1). For $T/T_0 = 0.86$, only after a short time evolution, the spectral peak vanishes due to strong diffusion induced by thermal fluctuations. We fit the structure factor with the Gaussian distribution $g(k) = A_0 \exp[-(k - k_d)^2/(2\sigma^2)]$, where A_0 , k_d , and σ are the fitting parameters. From k_d we determine the average domain size $L = 2\pi/k_d$. In Figs. 4(a2)–4(e2) we show the determined values of $L(t)$ on a log-log scale. The growth of $L(t)$ demonstrates a power-law behavior that is typical for coarsening of macroscopic domains $L \gg \xi_s$, where the spin healing length is defined as $\xi_s = \hbar/\sqrt{2mng_s}$, with $g_s = (2g_{12} - g_{11} - g_{22})/2$. ξ_s is a

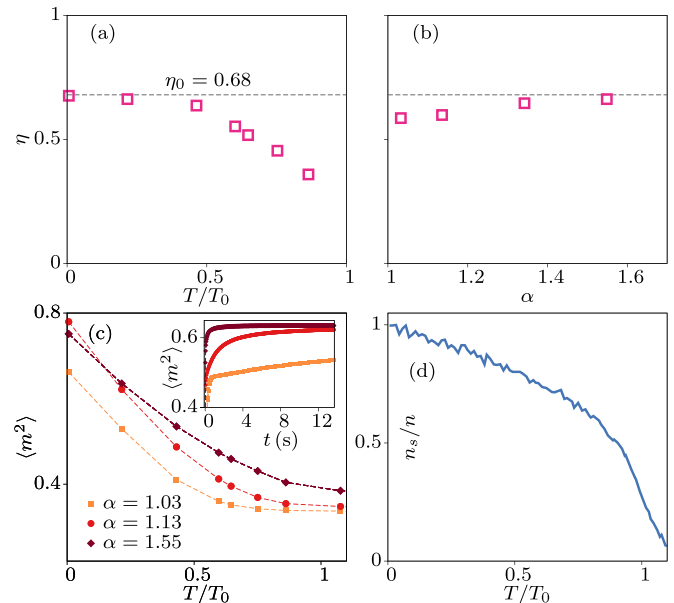


FIG. 5. Temperature and quench-parameter dependence. (a) $\eta(T)$ for $\alpha = 1.55$. (b) $\eta(\alpha)$ at $T/T_0 = 0.21$. The horizontal dashed line marks the zero-temperature prediction $\eta_0 = 0.68$. (c) Average squared imbalance $\langle m^2 \rangle$ at time $t = 11$ s as a function of T/T_0 for $\alpha = 1.03, 1.13,$ and 1.55 , while the inset shows the time evolution at $T/T_0 = 0.21$. (d) Temperature dependence of the initial superfluid fraction n_s/n , which we determine using the method described in Ref. [62]. The results are obtained for the system size $256 \times 256 \mu\text{m}^2$.

length scale on which the two species interact to nucleate domains. We extract a power law $f(t) = c_0 t^\eta$ with exponent η , with the assumption that the dependence scales as a power law. This way, we determine the scaling exponent η ; see caption of Fig. 4. We note that the value of η decreases with increasing temperature.

In Figs. 4(a3)–4(e3) we show the scaled structure factor $S(k, t)/L(t)^2$ as a function of the scaled wave vector $kL(t)$ for various t and T/T_0 . The different-time results collapse on one single curve, confirming the scaling hypothesis. The momentum tail follows a power-law behavior and its decay varies with temperature. For $T/T_0 = 0.21$ we find a dependence $S(k) \sim k^{-3}$, which is consistent with the Porod law [5]. This occurs due to the presence of domain walls that lead to the dependence $S(k) \sim k^{-3}$ at large k in 2D. At high temperature, the momentum tail decays slowly as the process of phase separation is suppressed by dominant thermal fluctuations. For $T/T_0 = 0.86$ we find a momentum-tail behavior $S(k) \sim k^{-1.25}$, where no phase separation is visible in the time evolution; see Appendix B.

Figures 5(a) and 5(b) show the temperature and quench-parameter dependence of the scaling exponent. Both T and α influence the value of η , exemplifying the interplay between strong and weak separation regimes. At low T and large α , the system is in the strong separation regime in the sense that the dynamics is marginally affected by initial fluctuations. Here we obtain η close to the zero-temperature prediction $\eta_0 = 0.68$, which suggests that the dominant process for domain growth is the inertial hydrodynamic transport of superfluid

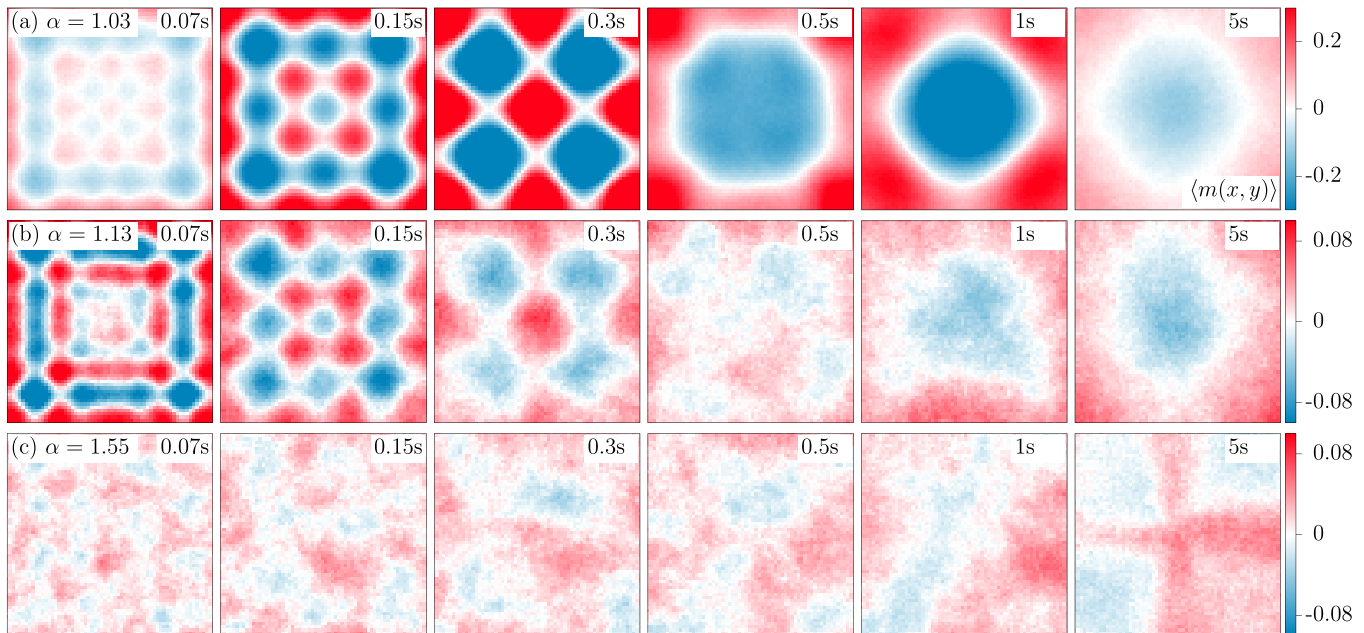


FIG. 6. Domain formation in a square box of size $64 \times 64 \mu\text{m}^2$. (a)–(c) show the time evolution of the average imbalance $\langle m(x, y) \rangle$ at $T/T_0 = 0.21$ for $\alpha = 1.03$ (upper row), 1.13 (middle row), and 1.55 (lower row). We present the full time evolution as videos in the Supplemental Material, which displays a continuous transformation between the domains of different shapes [63].

from low-density to high-density regions. This scenario is consistent with the simulations of binary condensates at zero temperature [50]. At high T and small α , initial fluctuations suppress the dynamics of phase separation and result in a modification of η and the high-momentum tail of the structure factor. We refer to this regime as the weak separation regime. To quantify these regimes we calculate the time evolution of the average squared imbalance $\langle m^2 \rangle$. In Fig. 5(c) we show $\langle m^2 \rangle$ at $t = 11$ s as a function of T/T_0 for $\alpha = 1.03, 1.13,$ and 1.55 . It decreases with increasing T/T_0 ; see also Appendix B. As shown in the inset of Fig. 5(c), $\langle m^2 \rangle$ increases during the time evolution and then slowly converges to the steady state in the long-time evolution. We find that the dynamics is in the strong separation regime for $\langle m^2 \rangle \gtrsim 0.64$, where we recover both the zero-temperature η_0 and the Porod tail of the structure factor. The weak separation regime sets in when $\langle m^2 \rangle \lesssim 0.64$, where thermal fluctuations modify the scaling parameters. Here the dynamics is influenced by thermal fluctuations that suppress the initial superfluid order of the system [Fig. 5(d)]. For $\langle m^2 \rangle \lesssim 0.4$ we observe no phase separation.

C. Demixing dynamics in a square box

We now turn to the demixing dynamics of a homogeneous 2D cloud confined in a square-box geometry, which is motivated by the experiments [51,52]. Compared to a periodic boundary system, where domain locations are spontaneous, finite boundaries break the translational invariance and act as a pinning potential for the formation of domains [26]. We choose the same density and the same quench protocol as above. We first analyze the demixing dynamics in a box cloud of size $64 \times 64 \mu\text{m}^2$, which is comparable to the experiments [51,52]. In Fig. 6 we show the time evolution of the average

imbalance $\langle m(x, y) \rangle$ at $T/T_0 = 0.21$ for $\alpha = 1.03, 1.13,$ and 1.55 . Indeed, the nucleation of domains is pinned by the box boundaries, which stems from a density difference at the edges since a_{11} and a_{22} are different, serving as a seed for the creation of domains. On the contrary, in the case of periodic-boundary systems domain nucleation is seeded from the fluctuations of the field. The box symmetry results in a qualitatively different average dynamics than in infinite systems. For $\alpha = 1.03$, the time evolution proceeds via formation of regular patterns that undergo a continuous transformation to create structures of striking, geometric shape. At $t \sim 0.5$ s the time evolution shows the creation of one macroscopic domain of components 1 and 2, which then equilibrates after $t \sim 5$ s. These results are close to the measurements that show the creation of similar structures for time evolution up to 100 ms

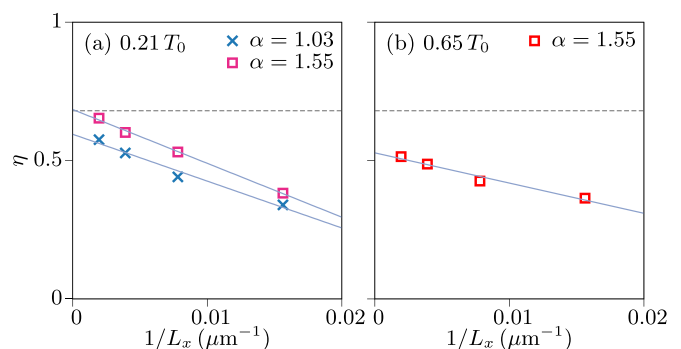


FIG. 7. Finite-size scaling. (a) η as a function of the inverse system length $1/L_x$ at $T/T_0 = 0.21$ for $\alpha = 1.03$ (crosses) and 1.55 (squares). The linear fit (continuous lines) yields $\eta_\infty = 0.59$ and 0.68 for $\alpha = 1.03$ and 1.55, respectively. (b) We obtain $\eta_\infty = 0.53$ at $T/T_0 = 0.65$ for $\alpha = 1.55$.

[51,52]. The pinning effect is suppressed when α is high; see the dynamics for $\alpha = 1.13$ and 1.55 in Figs. 6(b) and 6(c). The reason for this is the smaller spin healing length ξ_s at higher α , which supports the creation of small-sized domains. ξ_s is 4.6, 2.2, and 1.1 μm for $\alpha = 1.03, 1.13,$ and 1.55 , respectively. For the cloud size considered, we obtain $L_x/\xi_s \approx 14$ and 58 for $\alpha = 1.03$ and 1.55 , respectively, where the former supports the creation of regular-shaped domains due to the boundary condition. So, for $L_x/\xi_s \gg 1$, the dynamics approaches the one obtained for a system with periodic boundary conditions.

Next, we analyze the growth laws for the domains in a box cloud of sizes between $64 \times 64 \mu\text{m}^2$ and $512 \times 512 \mu\text{m}^2$. We calculate the structure factor $S(k, t)$ to determine the average domain size using the procedure described above. From the power-law growth of domains we ascertain the scaling exponent η , which is analogous to Fig. 4. In Fig. 7(a) we show η as a function of $1/L_x$ at $T/T_0 = 0.21$ for $\alpha = 1.03$ and 1.55 . L_x is the linear dimension of the box. The variation of system size by a factor of 64 allows us to perform a reliable finite-size scaling, which gives access to the scaling exponent η_∞ in the thermodynamic limit. We obtain $\eta_\infty = 0.59$ and 0.68 for $\alpha = 1.03$ and 1.55 , respectively. The results of η_∞ are close to the values obtained for periodic-boundary conditions. In Fig. 7(b) we show η as a function of $1/L_x$ at $T/T_0 = 0.65$ for $\alpha = 1.55$. For this system we find $\eta_\infty = 0.53$, confirming the suppression of the scaling exponent at high temperature.

IV. CONCLUSION

We have studied the demixing dynamics of a binary 2D Bose superfluid using classical-field simulations. By quenching the interspecies interaction parameter we have analyzed the coarsening dynamics at various values of temperature and the quench parameter. We have demonstrated that the dynamical scaling of domain growth interpolates between the inertial hydrodynamic growth law of binary fluids and the diffusive growth law of a 2D conserved field. Specifically, for low temperature and high quench we have found the inertial hydrodynamic growth law $L(t) \sim t^{2/3}$ and the Porod scaling law of the structure factor $S(k) \sim k^{-3}$, where L is the average domain size and k is the wave vector. We have pointed out that at high temperature thermal fluctuations suppress the demixing dynamics and modify both the domain growth law and the Porod tail of the structure factor. We have shown that near the superfluid transition temperature the scaling dynamics approaches the diffusive growth law of a 2D conserved field, $L(t) \sim t^{1/3}$, and the Porod tail scales similar to $S(k) \sim k^{-1}$. We have then studied the demixing dynamics in a box cloud. We have shown that for low quench and small clouds of sizes comparable to the spin healing length the box symmetry gives rise to distinctive dynamics, which is characterized by domains of geometric shapes. By varying the system size we have determined the scaling exponents of the growth law and found them to be consistent with the results of systems with periodic boundary conditions.

Our results highlight the fundamental interplay of the quench and thermal energy in phase separation, which mod-

ifies the underlying scaling laws of coarsening dynamics. We note that these considerations might apply to the recent results reported in [64]. The experimental realization of our results provides a quantum simulation of scaling laws of binary fluids. Furthermore, Bose mixtures in a ring trap offer the capability to study the solid-body rotation and persistent currents in multicomponent quantum mixtures.

ACKNOWLEDGMENTS

We thank Jean Dalibard and Raphaël Saint-Jalm for inspiring discussions. L.M. acknowledges funding by the Deutsche Forschungsgemeinschaft (DFG) in the framework of SFB 925, Project ID 170620586, and the excellence cluster ‘‘Advanced Imaging of Matter,’’ EXC 2056, Project ID 390715994.

APPENDIX A: MOMENTUM RANGE OF UNSTABLE MODES

The range of unstable modes is obtained by setting $E_{k,-} = 0$ in Eq. (8), which results in

$$\left(\frac{\epsilon_k}{g_{11}n_1} + 2\right)\left(\frac{\epsilon_k}{g_{22}n_2} + 2\right) = 4\alpha^2. \quad (\text{A1})$$

For the continuum free-particle dispersion $\epsilon_k = \hbar^2 k^2 / (2m)$, Eq. (A1) becomes

$$(k^2 \xi_1^2 + 2)(k^2 \xi_2^2 + 2) = 4\alpha^2, \quad (\text{A2})$$

where $\xi_a = \hbar / \sqrt{2mg_{aa}n_a}$ are the healing lengths, with $a = 1, 2$. We solve Eq. (A2) for k and obtain the solution

$$k_0^2 = \frac{1}{\xi_1^2 \xi_2^2} \left[\sqrt{(\xi_1^2 - \xi_2^2)^2 + 4\alpha^2 \xi_1^2 \xi_2^2} - (\xi_1^2 + \xi_2^2) \right]. \quad (\text{A3})$$

For the discrete free-particle dispersion $\epsilon_k = 4J \sin^2(kl/2)$, with $J = \hbar^2 / (2ml^2)$, Eq. (A1) takes the form

$$[4\tilde{\xi}_1^2 \sin^2(\tilde{k}/2) + 2][4\tilde{\xi}_2^2 \sin^2(\tilde{k}/2) + 2] = 4\alpha^2, \quad (\text{A4})$$

where $\tilde{\xi}_1 = \xi_1/l$, $\tilde{\xi}_2 = \xi_2/l$, $\tilde{k} = kl$, and l is the lattice discretization length. For small \tilde{k} , $\sin^2(\tilde{k}/2) \approx \tilde{k}^2/4$ and we recover Eq. (A2) and the result in Eq. (A3). This is the reason why the result of k_0 differs for large α in Fig. 3, where large α leads to a large value of k_0 and hence the deviation from the discretized dispersion relation.

APPENDIX B: INFLUENCE OF TEMPERATURE ON THE DEMIXING DYNAMICS

In this section we show how the thermal fluctuations suppress the demixing dynamics at nonzero temperatures. We calculate the imbalance $m(x, y)$ of a single sample of the ensemble for the immiscible parameter $\alpha = 1.55$ and the system size of $256 \times 256 \mu\text{m}^2$. In Fig. 8 we show the time evolution of $m(x, y)$ for various values of the temperature T/T_0 . The coarsening dynamics is affected by the initial thermal fluctuations, resulting in a suppression of phase separation at high temperatures. Near the superfluid critical

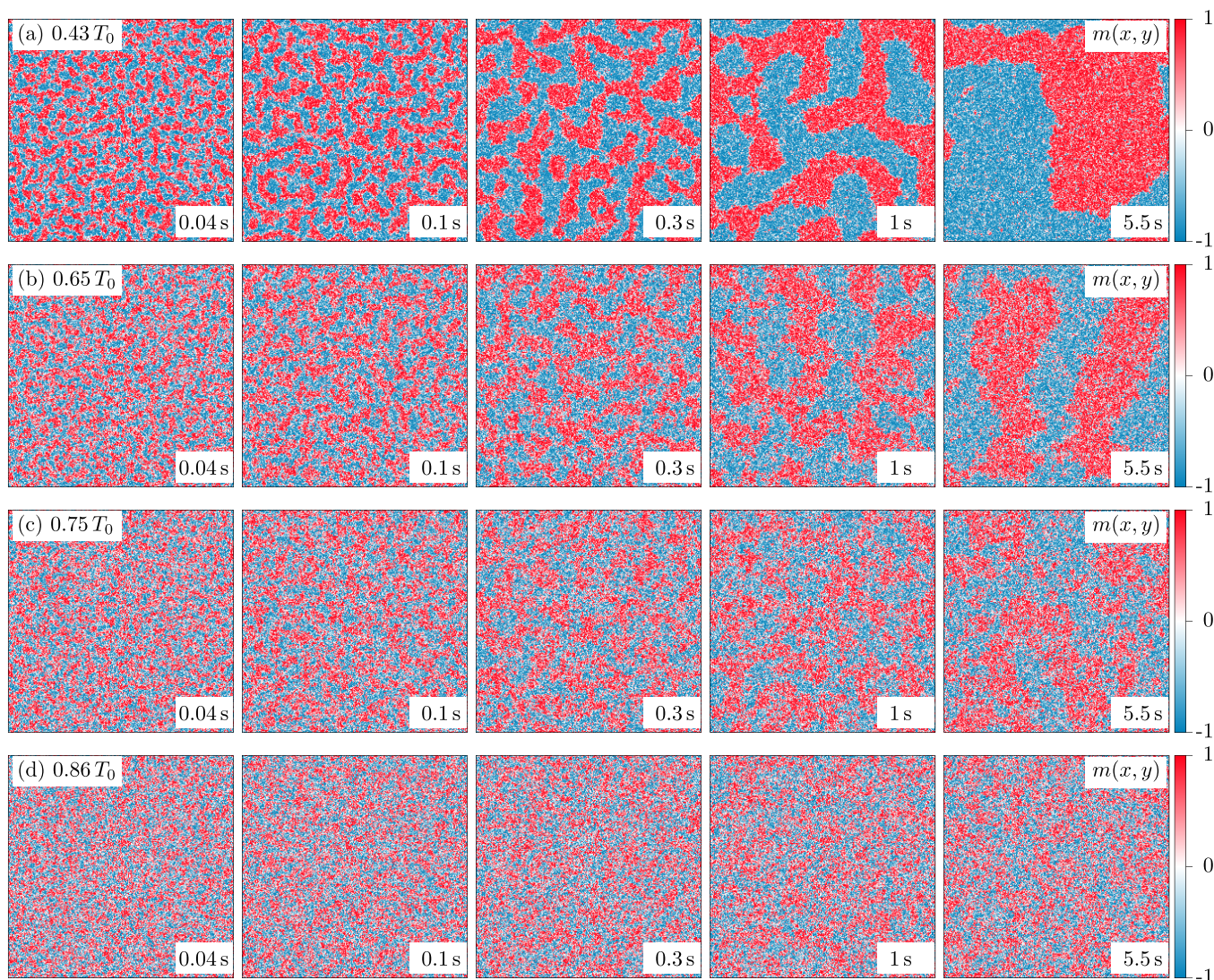


FIG. 8. Influence of temperature on the demixing dynamics in a periodic-boundary system of size $256 \times 256 \mu\text{m}^2$ for $\alpha = 1.55$. (a)–(d) show the time evolution of the imbalance $m(x, y)$ of a single trajectory after the quench deep in the demixed state at temperatures $T/T_0 = 0.43, 0.65, 0.75,$ and 0.86 . The red and blue colors denote the two components.

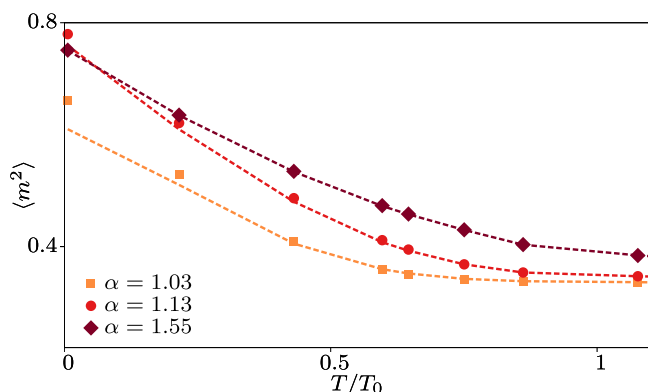


FIG. 9. Average squared imbalance $\langle m^2 \rangle$ as a function of temperature T/T_0 , determined from the time evolution at $t = 5.5$ s (dashed lines) and 11 s (symbols).

temperature at $T/T_0 = 0.86$ we find no distinguishable phase separation.

As shown in Fig. 2 the long-time relaxation is slow for $\alpha = 1.03$ compared to the dynamics for $\alpha = 1.55$. This is also reflected in the values of the average squared imbalance $\langle m^2 \rangle$ in Fig. 9, which shows the temperature dependence of $\langle m^2(t) \rangle$ determined at two different times $t = 5.5$ s and 11 s in the time evolution. This confirms that the long-time relaxation is slow for small α at low temperatures, whereas dominant thermal fluctuations facilitate relaxation for systems at high temperatures.

APPENDIX C: NONEQUILIBRIUM EXCITATION SPECTRA

In Fig. 10 we show the results of the dynamic structure factor $S_1(\mathbf{k}, \omega)$, which are calculated using a longer sampling

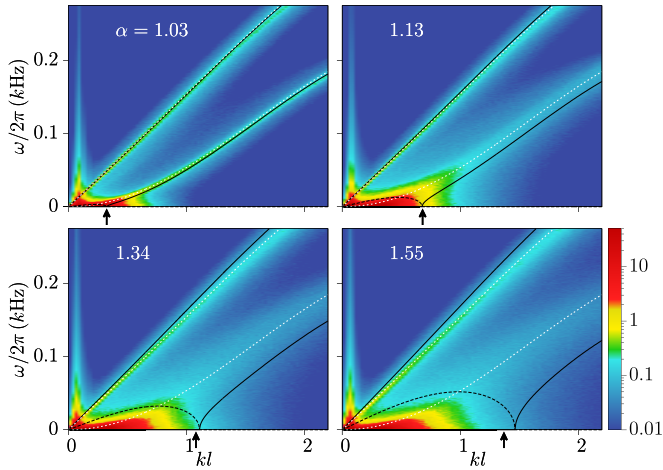


FIG. 10. Dynamic structure factor $S_1(\mathbf{k}, \omega)$ as a function of the wave vector $\mathbf{k} = k\hat{\mathbf{x}}$ and frequency ω for $\alpha = 1.03, 1.13, 1.34,$ and 1.55 , which is determined using a longer sampling time of $T_s = 1.1$ s. The black continuous lines, the black dashed line, and the white dotted lines are the same as in Fig. 3. The arrow indicates the momentum range of unstable modes based on Eq. (A3).

time of $T_s = 1.1$ s. The overall features of the excitation spectra are similar to the results of sampling time of $T_s = 0.55$ s presented in Fig. 3.

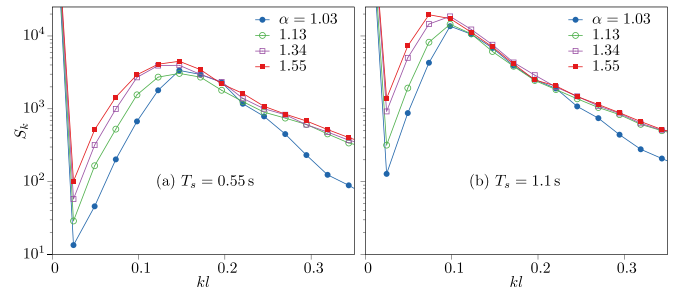


FIG. 11. Structure factor S_k as a function of the wave vector $\mathbf{k} = k\hat{\mathbf{x}}$ for $\alpha = 1.03, 1.13, 1.34,$ and 1.55 , determined using two sampling times: (a) $T_s = 0.55$ s and (b) $T_s = 1.1$ s.

As we mention in the main text, $S_1(\mathbf{k}, \omega)$ displays a peaklike excitation at low wave vector k corresponding to a macroscopic domain that the system forms at the sampling time T_s . To show that the location of this peak changes with α , we determine the structure factor $S_k = \sum_{\omega} S_1(\mathbf{k}, \omega)$ from the results of $S_1(\mathbf{k}, \omega)$. In Fig. 11 we plot S_k as a function of k for $\alpha = 1.03, 1.13, 1.34,$ and 1.55 . The peak occurs at a lower k for high α . Furthermore, there is an overall shift in the peak location depending on the sampling time T_s . We note that the rapid growth of S_k at $k = 0$ refers to the condensate mode.

- [1] A. Onuki, *Phase Transition Dynamics* (Cambridge University Press, Cambridge, 2002).
- [2] M. Tateno and H. Tanaka, Power-law coarsening in network-forming phase separation governed by mechanical relaxation, *Nat. Commun.* **12**, 912 (2021).
- [3] B. Wang, L. Zhang, T. Dai, Z. Qin, H. Lu, L. Zhang, and F. Zhou, Liquid-liquid phase separation in human health and diseases, *Signal Transduct. Target. Ther.* **6**, 290 (2021).
- [4] S. Mehta and J. Zhang, Liquid-liquid phase separation drives cellular function and dysfunction in cancer, *Nat. Rev. Cancer* **22**, 239 (2022).
- [5] A. J. Bray, Theory of phase-ordering kinetics, *Adv. Phys.* **43**, 357 (1994).
- [6] P. Debye Jr., H. R. Anderson, and H. Brumberger, Scattering by an inhomogeneous solid. II. The correlation function and its application, *J. Appl. Phys.* **28**, 679 (1957).
- [7] I. M. Lifshitz and V. V. Slyozov, The kinetics of precipitation from supersaturated solid solutions, *J. Phys. Chem. Solids* **19**, 35 (1961).
- [8] D. A. Huse, Corrections to late-stage behavior in spinodal decomposition: Lifshitz-Slyozov scaling and Monte Carlo simulations, *Phys. Rev. B* **34**, 7845 (1986).
- [9] E. D. Siggia, Late stages of spinodal decomposition in binary mixtures, *Phys. Rev. A* **20**, 595 (1979).
- [10] H. Furukawa, Effect of inertia on droplet growth in a fluid, *Phys. Rev. A* **31**, 1103 (1985).
- [11] V. P. Mineev, The theory of the solution of two near-ideal Bose gases, *Zh. Eksp. Teor. Fiz.* **67**, 263 (1974) [*Sov. Phys. -JETP* **40**, 132 (1974)].
- [12] T.-L. Ho and V. B. Shenoy, Binary mixtures of Bose condensates of alkali atoms, *Phys. Rev. Lett.* **77**, 3276 (1996).
- [13] E. Timmermans, Phase separation of Bose-Einstein condensates, *Phys. Rev. Lett.* **81**, 5718 (1998).
- [14] H. Pu and N. P. Bigelow, Properties of two-species Bose condensates, *Phys. Rev. Lett.* **80**, 1130 (1998).
- [15] D. S. Hall, M. R. Matthews, J. R. Ensher, C. E. Wieman, and E. A. Cornell, Dynamics of component separation in a binary mixture of Bose-Einstein condensates, *Phys. Rev. Lett.* **81**, 1539 (1998).
- [16] S. B. Papp, J. M. Pino, and C. E. Wieman, Tunable miscibility in a dual-species Bose-Einstein condensate, *Phys. Rev. Lett.* **101**, 040402 (2008).
- [17] D. J. McCarron, H. W. Cho, D. L. Jenkin, M. P. Köpinger, and S. L. Cornish, Dual-species Bose-Einstein condensate of ^{87}Rb and ^{133}Cs , *Phys. Rev. A* **84**, 011603(R) (2011).
- [18] L. Wacker, N. B. Jørgensen, D. Birkmose, R. Horchani, W. Ertmer, C. Klempt, N. Winter, J. Sherson, and J. J. Arlt, Tunable dual-species Bose-Einstein condensates of ^{39}K and ^{87}Rb , *Phys. Rev. A* **92**, 053602 (2015).
- [19] P. Maddaloni, M. Modugno, C. Fort, F. Minardi, and M. Inguscio, Collective oscillations of two colliding Bose-Einstein condensates, *Phys. Rev. Lett.* **85**, 2413 (2000).
- [20] K. M. Mertes, J. W. Merrill, R. Carretero-González, D. J. Frantzeskakis, P. G. Kevrekidis, and D. S. Hall, Nonequilibrium dynamics and superfluid ring excitations in binary Bose-Einstein condensates, *Phys. Rev. Lett.* **99**, 190402 (2007).
- [21] Y. Eto, M. Takahashi, K. Nabeta, R. Okada, M. Kunimi, H. Saito, and T. Hirano, Bouncing motion and penetration dynamics in multicomponent Bose-Einstein condensates, *Phys. Rev. A* **93**, 033615 (2016).

- [22] Y. Eto, M. Takahashi, M. Kunimi, H. Saito, and T. Hirano, Nonequilibrium dynamics induced by miscible-immiscible transition in binary Bose-Einstein condensates, *New J. Phys.* **18**, 073029 (2016).
- [23] C. Hamner, J. J. Chang, P. Engels, and M. A. Hoefer, Generation of dark-bright soliton trains in superfluid-superfluid counterflow, *Phys. Rev. Lett.* **106**, 065302 (2011).
- [24] M. A. Hoefer, J. J. Chang, C. Hamner, and P. Engels, Dark-dark solitons and modulational instability in miscible two-component Bose-Einstein condensates, *Phys. Rev. A* **84**, 041605(R) (2011).
- [25] B. Bakkali-Hassani, C. Maury, Y.-Q. Zou, É. Le Cerf, R. Saint-Jalm, P. C. M. Castilho, S. Nascimbene, J. Dalibard, and J. Beugnon, Realization of a townes soliton in a two-component planar Bose gas, *Phys. Rev. Lett.* **127**, 023603 (2021).
- [26] S. De, D. L. Campbell, R. M. Price, A. Putra, B. M. Anderson, and I. B. Spielman, Quenched binary Bose-Einstein condensates: Spin-domain formation and coarsening, *Phys. Rev. A* **89**, 033631 (2014).
- [27] J. Sabbatini, W. H. Zurek, and M. J. Davis, Phase Separation and Pattern Formation in a Binary Bose-Einstein Condensate, *Phys. Rev. Lett.* **107**, 230402 (2011).
- [28] E. Nicklas, H. Strobel, T. Zibold, C. Gross, B. A. Malomed, P. G. Kevrekidis, and M. K. Oberthaler, Rabi flopping induces spatial demixing dynamics, *Phys. Rev. Lett.* **107**, 193001 (2011).
- [29] E. Nicklas, M. Karl, M. Höfer, A. Johnson, W. Muessel, H. Strobel, J. Tomkovič, T. Gasenzer, and M. K. Oberthaler, Observation of scaling in the dynamics of a strongly quenched quantum gas, *Phys. Rev. Lett.* **115**, 245301 (2015).
- [30] K. Damle, S. N. Majumdar, and S. Sachdev, Phase ordering kinetics of the Bose gas, *Phys. Rev. A* **54**, 5037 (1996).
- [31] S. Mukerjee, C. Xu, and J. E. Moore, Dynamical models and the phase ordering kinetics of the $s = 1$ spinor condensate, *Phys. Rev. B* **76**, 104519 (2007).
- [32] H. Takeuchi, K. Kasamatsu, M. Tsubota, and M. Nitta, Tachyon condensation due to domain-wall annihilation in Bose-Einstein condensates, *Phys. Rev. Lett.* **109**, 245301 (2012).
- [33] M. Karl, B. Nowak, and T. Gasenzer, Universal scaling at non-thermal fixed points of a two-component Bose gas, *Phys. Rev. A* **88**, 063615 (2013).
- [34] K. Kudo and Y. Kawaguchi, Magnetic domain growth in a ferromagnetic Bose-Einstein condensate: Effects of current, *Phys. Rev. A* **88**, 013630 (2013).
- [35] K. Kudo and Y. Kawaguchi, Coarsening dynamics driven by vortex-antivortex annihilation in ferromagnetic Bose-Einstein condensates, *Phys. Rev. A* **91**, 053609 (2015).
- [36] L. A. Williamson and P. B. Blakie, Universal coarsening dynamics of a quenched ferromagnetic spin-1 condensate, *Phys. Rev. Lett.* **116**, 025301 (2016).
- [37] L. A. Williamson and P. B. Blakie, Coarsening and thermalization properties of a quenched ferromagnetic spin-1 condensate, *Phys. Rev. A* **94**, 023608 (2016).
- [38] H. Takeuchi, Domain-area distribution anomaly in segregating multicomponent superfluids, *Phys. Rev. A* **97**, 013617 (2018).
- [39] K. Fujimoto, K. Haneda, K. Kudo, and Y. Kawaguchi, Scale-invariant relaxation dynamics in two-component Bose-Einstein condensates with large particle-number imbalance, *Phys. Rev. A* **101**, 023608 (2020).
- [40] K. Kasamatsu and M. Tsubota, Multiple domain formation induced by modulation instability in two-component Bose-Einstein condensates, *Phys. Rev. Lett.* **93**, 100402 (2004).
- [41] K. Kasamatsu and M. Tsubota, Modulation instability and solitary-wave formation in two-component Bose-Einstein condensates, *Phys. Rev. A* **74**, 013617 (2006).
- [42] K. Sasaki, N. Suzuki, D. Akamatsu, and H. Saito, Rayleigh-Taylor instability and mushroom-pattern formation in a two-component Bose-Einstein condensate, *Phys. Rev. A* **80**, 063611 (2009).
- [43] H. Takeuchi, N. Suzuki, K. Kasamatsu, H. Saito, and M. Tsubota, Quantum Kelvin-Helmholtz instability in phase-separated two-component Bose-Einstein condensates, *Phys. Rev. B* **81**, 094517 (2010).
- [44] N. Suzuki, H. Takeuchi, K. Kasamatsu, M. Tsubota, and H. Saito, Crossover between Kelvin-Helmholtz and counter-superflow instabilities in two-component Bose-Einstein condensates, *Phys. Rev. A* **82**, 063604 (2010).
- [45] K. Sasaki, N. Suzuki, and H. Saito, Dynamics of bubbles in a two-component Bose-Einstein condensate, *Phys. Rev. A* **83**, 033602 (2011).
- [46] K. Sasaki, N. Suzuki, and H. Saito, Capillary instability in a two-component Bose-Einstein condensate, *Phys. Rev. A* **83**, 053606 (2011).
- [47] B. Van Schaeybroeck, Weakly interacting Bose mixtures at finite temperature, *Physica A* **392**, 3806 (2013).
- [48] A. Roy and D. Angom, Thermal suppression of phase separation in condensate mixtures, *Phys. Rev. A* **92**, 011601(R) (2015).
- [49] K. L. Lee, N. B. Jørgensen, I.-K. Liu, L. Wacker, J. J. Arlt, and N. P. Proukakis, Phase separation and dynamics of two-component Bose-Einstein condensates, *Phys. Rev. A* **94**, 013602 (2016).
- [50] J. Hofmann, S. S. Natu, and S. Das Sarma, Coarsening dynamics of binary Bose condensates, *Phys. Rev. Lett.* **113**, 095702 (2014).
- [51] R. Saint-Jalm, Exploring two-dimensional physics with Bose gases in box potentials: Phase ordering and dynamical symmetry, Ph.D. thesis, Université Paris Sciences et Lettres, 2019.
- [52] E. Le Cerf, Demixing phenomena in 2D Bose gases, Ph.D. thesis, Sorbonne Université, 2020.
- [53] A. Widera, F. Gerbier, S. Fölling, T. Gericke, O. Mandel, and I. Bloch, Precision measurement of spin-dependent interaction strengths for spin-1 and spin-2 ^{87}Rb atoms, *New J. Phys.* **8**, 152 (2006).
- [54] P. A. Altin, G. McDonald, D. Döring, J. E. Debs, T. H. Barter, N. P. Robins, J. D. Close, S. A. Haine, T. M. Hanna, and R. P. Anderson, Optically trapped atom interferometry using the clock transition of large ^{87}Rb Bose-Einstein condensates, *New J. Phys.* **13**, 119401 (2011).
- [55] C. J. Pethick and H. Smith, *Bose-Einstein Condensation in Dilute Gases*, 2nd ed. (Cambridge University Press, Cambridge, 2008).
- [56] V. P. Singh, W. Weimer, K. Morgener, J. Siegl, K. Hueck, N. Luick, H. Moritz, and L. Mathey, Probing superfluidity of Bose-Einstein condensates via laser stirring, *Phys. Rev. A* **93**, 023634 (2016).

- [57] V. P. Singh, C. Weitenberg, J. Dalibard, and L. Mathey, Superfluidity and relaxation dynamics of a laser-stirred two-dimensional Bose gas, *Phys. Rev. A* **95**, 043631 (2017).
- [58] C. Mora and Y. Castin, Extension of Bogoliubov theory to quasicondensates, *Phys. Rev. A* **67**, 053615 (2003).
- [59] N. Prokof'ev, O. Ruebenacker, and B. Svistunov, Critical point of a weakly interacting two-dimensional Bose gas, *Phys. Rev. Lett.* **87**, 270402 (2001).
- [60] N. Prokof'ev and B. Svistunov, Two-dimensional weakly interacting Bose gas in the fluctuation region, *Phys. Rev. A* **66**, 043608 (2002).
- [61] L. Mathey, K. J. Günter, J. Dalibard, and A. Polkovnikov, Dynamic Kosterlitz-Thouless transition in two-dimensional Bose mixtures of ultracold atoms, *Phys. Rev. A* **95**, 053630 (2017).
- [62] V. P. Singh and L. Mathey, Collective modes and superfluidity of a two-dimensional ultracold Bose gas, *Phys. Rev. Res.* **3**, 023112 (2021).
- [63] See Supplemental Material at <http://link.aps.org/supplemental/10.1103/PhysRevResearch.5.043042> for animation of dynamics of phase separation in a box cloud.
- [64] S. Huh, K. Mukherjee, K. Kwon, J. Seo, S. I. Mistakidis, H. R. Sadeghpour, and J. Yoon Choi, Classifying the universal coarsening dynamics of a quenched ferromagnetic condensate, [arXiv:2303.05230](https://arxiv.org/abs/2303.05230).